Spin chirality induced large topological Hall effect in magnetic Weyl semimetallic Eu$_2$Ir$_2$O$_7$(111) thin films

Mithun Ghosh [1], D. Samal,[2,3] and P. S. Anil Kumar [1]

[1]*Department of Physics, Indian Institute of Science, Bangalore 560012, Karnataka, India*
[2]*Institute of Physics, Sachivalaya Marg, Bhubaneswar 751005, India*
[3]*Homi Bhabha National Institute, Anushakti Nagar, Mumbai 400085, India*

Antiferromagnetic (AFM) pyrochlore iridates are a fertile ground to hunt for a Weyl semimetallic state characterized by a linear crossing of two nondegenerate bands near the Fermi level E_F. Here, we demonstrate evidence of low-temperature anomalous and topological Hall effects in an antiferromagnetic Eu$_2$Ir$_2$O$_7$(111) epitaxial thin film. The observed anomalous Hall effect is explained in terms of the momentum space Berry curvature associated with the Weyl nodes in the electronic band structure. The topological Hall effect reaches a large value $\rho_{xy}^{\mathrm{THE}} \sim 10\,\mu\Omega\,\mathrm{cm}$ at 2 K. The topological nature of the Hall effect is attributed to the nonzero scalar spin chirality of the all-in-all-out/all-out-all-in (AIAO/AOAI) type noncoplanar AFM spin structure. The magnetoresistance (MR) shows a prominent negative variation (MR $\sim 10\%$ at 2 K) below 10 K. The field dependence of MR below 5 K varies quadratically in the low-field regime, and above 40 kOe it shows a linear trend. The quadratic to linear crossover of the MR is explained by the field-induced (H) spin canting (spin chirality) of the static spins in the AIAO/AOAI spin structure. In the intermediate-temperature region MR of $15-25$ K exhibits a hysteretic response which is associated with field-induced domain switching of the AIAO/AOAI spin structure. This work highlights the interplay of magnetism and topology in a spin-orbit-coupled correlated electron system and unravels the possibility for realizing the Weyl phase in antiferromagnetic Eu$_2$Ir$_2$O$_7$(111) thin films.

I. INTRODUCTION

Recently, the focus of condensed-matter research has undergone a paradigm shift towards the realization of topologically nontrivial electronic phases in spin-orbit-coupled correlated materials [1–5]. Of particular interest are Weyl semimetals (WSMs), in which two nondegenerate bulk bands cross linearly at the band-touching points (Weyl nodes) and the low-energy electronic excitation is characterized by Weyl fermions. They also exhibit a Fermi-arc surface state in the three-dimensional (3D) Brillouin zone that is evident from photoemission spectroscopy [6–8]. The Weyl node acts as a source or drain of Berry curvature (the quantum mechanical Berry phase) or the magnetic monopole in momentum space [6,9]. The Berry phase of the electronic wave function has a profound effect on the magnetotransport properties of materials [10,11]. Due to the nontrivial 3D band structure, WSMs in an applied magnetic field show a number of anomalous transport phenomena, like the anomalous Nernst effect [12], the Adler-Bell-Jackiw anomaly (or chiral anomaly) [13], and the anomalous Hall effect (AHE) [14,15]. Experimentally, the WSM phase can be realized either in broken time-reversal symmetry (magnetic) or space-inversion symmetry (noncentrosymmetric) systems [8]. So far, many of the WSM phases have been realized in with broken inversion symmetry [8]. However, there are a few cases of time-reversal-breaking magnetic systems like Co$_3$Sn$_2$S$_2$ [16,17], Co$_2$MnGa [18], and Mn$_3$Sn [19], which are experimentally found to host a WSM state as well.

In realistic parameter regions, theoretical *ab initio* calculations have predicted the realization of the magnetic WSM phase in pyrochlore iridates A_2Ir$_2$O$_7$ (where A is Y or a rare-earth element) [6,14,20]. In pyrochlore iridates, the WSM phase can be stabilized by the broken time-reversal symmetry of the all-in-all-out/all-out-all-in (AIAO/AOAI) antiferromagnetic (AFM) ordering [21]. Among the pyrochlore iridates Eu$_2$Ir$_2$O$_7$ has received considerable interest since it is predicted to host the WSM phase [22]. Theoretical calculations for WSMs predict a nonquantized anomalous Hall conductance $\sigma_{xy}^{\mathrm{AHE}}$, the value of which is proportional to the separation of the Weyl nodes in momentum space [8, 23–25]. Although the AIAO/AOAI spin structure has been experimentally verified [26,27], the observation of an intrinsic AHE effect remains unexplored in bulk Eu$_2$Ir$_2$O$_7$. Since bulk cubic Eu$_2$Ir$_2$O$_7$ preserves all three C_2 symmetries, the net Berry curvature $\Omega(\vec{k})$ contribution cancels out [28]. So to realize an intrinsic AHE originating from the Weyl nodes, the bulk cubic symmetry needs to be broken. One easy way to break the cubic symmetry is by introducing epitaxial strain in thin films. Therefore, strained Eu$_2$Ir$_2$O$_7$(111) thin films with an AIAO/AOAI magnetic order are found to be an ideal platform to realize the theoretically predicted WSM phase for investigating the existence of an intrinsic AHE. Further, because of the noncoplanar AIAO/AOAI-type spin structure induced by geometrical frustration in the pyrochlore lattice [27], Eu$_2$Ir$_2$O$_7$ is expected to exhibit a large scalar spin chirality χ_{ijk} [29–32]. The spin chirality can lead to nontrivial transport phenomena like the topological Hall
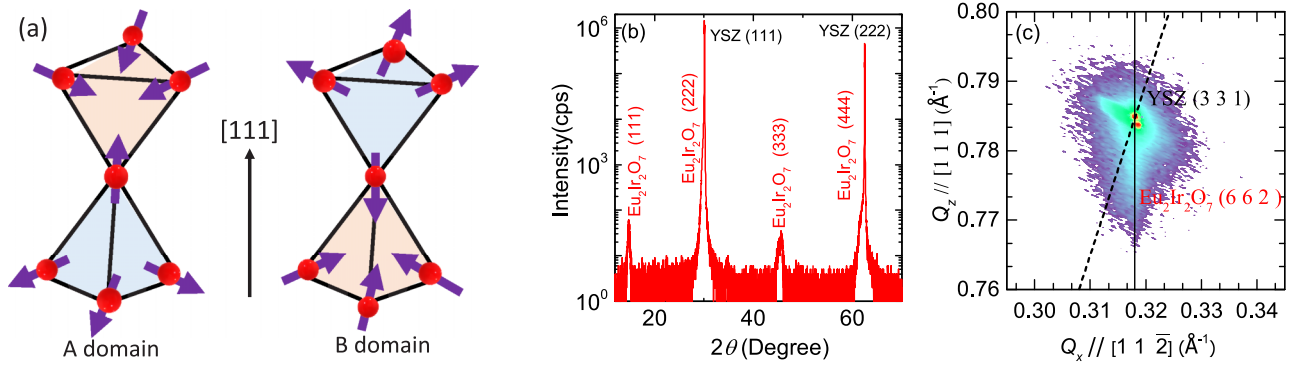
FIG. 1. (a) Schematic magnetic configuration of the all-in-all-out/all-out-all-in state for domain A (left) and domain B (right). (b) XRD θ-2θ scan of a $Eu_2Ir_2O_7$(111) thin film. (c) Asymmetric RSM scan around YSZ(331) and the $Eu_2Ir_2O_7$(662) peak. The vertical solid line indicates coherent growth of $Eu_2Ir_2O_7$ on YSZ(111). The dashed line passing through the origin of Q_x-Q_z plot corresponds to relaxed cubic growth.

effect (THE) and large negative magnetoresistance (MR) [33]. The topological Hall effect arises when a conduction electron acquires quantum mechanical Berry curvature associated with the real-space spin chirality. In contrast to the AHE, spin-orbit coupling is not necessary to observe the THE [34].

Most of the electronic properties of magnetic materials are governed by their underlying spin structure. The AIAO/AOAI (four-in-four-out) type ground state ($H = 0$) magnetic order of $Eu_2Ir_2O_7$ generally has two kinds of magnetic domains: domain A, in which all spins at the vertices of the tetrahedra are pointed towards the center, and domain B, in which they are pointed away from the center [shown in Fig. 1(a)]. At zero magnetic field, a sample will have both domains A and B in equal amounts. But $Eu_2Ir_2O_7$ has uniaxial magnetic anisotropy along the [111] direction. Therefore, an applied external magnetic field can cause flipping of the spins and leads to a switching from domain A to domain B and vice versa depending upon the field direction [35,36]. The field-induced spin flipping (domain switching) phenomenon is decided by the competition between the Zeeman energy and antiferromagnetic exchange energy of the Ir^{4+} ($J_{eff} = 1/2$) moments [21]. Therefore, $Eu_2Ir_2O_7$ can have an odd-even magnetic domain distribution depending upon the temperature T and applied magnetic field H values. The field-induced modification of the domain configuration can lead to many interesting transport phenomena like the negative to positive crossover and hysteresis in MR [35,36]. Therefore, the temperature T and magnetic field H dependence is highly indispensable in a systematic magnetotransport study of $Eu_2Ir_2O_7$ thin films.

In view of the above discussion, the observation of a magnetic WSM phase in the pyrochlore iridate $Eu_2Ir_2O_7$ will be interesting because of its AIAO/AOAI noncoplanar spin structure and topologically nontrivial electronic band structure. In this paper, we carry out an in-depth magnetotransport study in a biaxially strained $Eu_2Ir_2O_7$(111) thin film ($\sim$55 nm) epitaxially grown on the Y_2O_3 stabilized ZrO_2 (YSZ) (111) substrate. Observation of a large intrinsic AHE signifies that $Eu_2Ir_2O_7$(111) thin films host the WSM phase in their AIAO/AOAI AFM ordered phase. The observation of THE and large negative MR in the low-temperature region (2−5 K) signifies the presence of noncoplanar spin textures with scalar spin chirality.

II. EXPERIMENTAL DETAILS

The $Eu_2Ir_2O_7$(111) epitaxial thin film is fabricated by means of a two-step solid-phase epitaxy technique using the pulsed laser deposition technique. The details of the sample preparation were discussed in an earlier report [37]. The crystallinity of the $Eu_2Ir_2O_7$ thin films was characterized using a Rigaku SmartLab high-resolution four-circle x-ray diffractometer (Cu $K\alpha_1$ radiation). The electrical and magnetotransport properties were measured using a physical property measurement system (Quantum Designs) on a standard Hall bar structure (190×100 μm^2) fabricated by photolithography followed by Ar ion etching. Cr/Au (10/70 nm) contact pads were deposited by an e-beam evaporator on top of the films to have Ohmic contact with devices. To provide electrical contact, Al (25 μm diameter) wire is bonded on the Cr/Au pads by means of ultrasonic vibration using a TPT wire bonding tool.

III. EXPERIMENTAL RESULTS AND DISCUSSION

A. Epitaxial growth of $Eu_2Ir_2O_7$

Figure 1(b) shows an x-ray diffraction (XRD) θ-2θ scan of the postannealed $Eu_2Ir_2O_7$ thin film; it shows the presence of only a (111)-oriented peak of $Eu_2Ir_2O_7$. The presence of odd-numbered peaks confirms the pyrochlore structure of space group $Fd\bar{3}m$. The asymmetric reciprocal space mapping (RSM) around YSZ(331) and $Eu_2Ir_2O_7$(662) is plotted in Fig. 1(c). The tail of the $Eu_2Ir_2O_7$(662) peak along the Q_z axis indicates coherent growth of $Eu_2Ir_2O_7$ on the YSZ substrate.

B. Longitudinal resistivity

The temperature dependence of the longitudinal resistivity ρ_{xx} is plotted in Fig. 2(a). It shows a metallic behavior ($d\rho/dT > 0$) from 300 down to 90 K, below which the resistivity increases ($d\rho/dT < 0$) down to the lowest measured temperature of 2 K. The resulting conductivity σ_{xx} at 2 K has a value of $\sim$21 Ω^{-1} cm^{-1}. The transition at 90 K is associated with the thermally driven metal-semimetal transition. The low inverse residual resistivity ratio of 3.6 and a
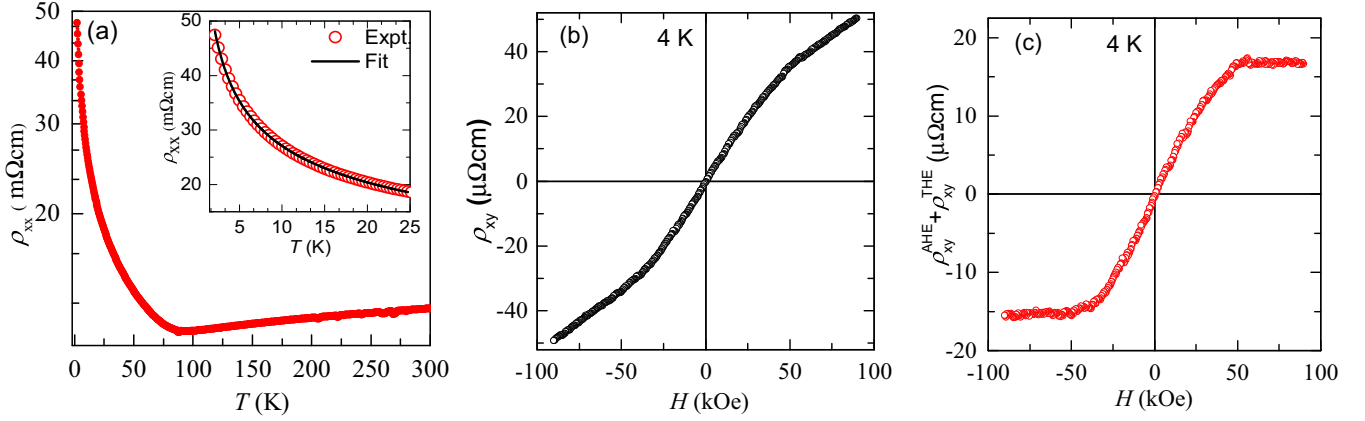
FIG. 2. (a) Temperature dependence of the longitudinal resistivity ρ_{xx}, which shows a clear metal-semimetal transition around 90 K; the inset shows power-law fitting in the temperature range of $2-25$ K. (b) The antisymmetric Hall resistivity ρ_{xy} data extracted from the raw Hall data at 4 K. (c) Extra component of the Hall resistivity after subtracting the ordinary Hall resistivity component from the total Hall resistivity ρ_{xy}, as shown in (b).

decrease in transition temperature (bulk transition temperature of 120 K) could be related to a slight Ir excess in the films [37]. The low-temperature ($2-25$ K) resistivity data follow a power-law dependence on temperature $\rho = a + bT^{-\alpha}$, with the exponent $\alpha \sim 0.3$ [shown in the inset of Fig. 2(a)], which signifies a semimetallic charge transport with vanishing conductivity as $T \rightarrow 0$ K [6].

C. Anomalous Hall effects

Magnetotransport measurements reflect versatile information about the orbital motion, spin states, and band structure of the conduction electrons. These measurements were performed on an L-shaped Hall bar of a $Eu_2Ir_2O_7(111)$ epitaxial thin film with a thickness of 55 nm. During the measurements, magnetic field H was applied along the [111] direction, and current I was applied along either the [1$\bar{1}$0] or [11$\bar{2}$] direction; that is, always, $I \perp H$ for both current directions (Hall bar). Here, we present Hall data for one of the Hall bars. Figure 2(b) shows the Hall resistivity ρ_{xy} data at 4 K. The Hall data were antisymmetrized to eliminate the magnetoresistance contribution, i.e.,

$$\rho_{xy}(H) = \frac{\rho_{xy}^{raw}(+H) - \rho_{xy}^{raw}(-H)}{2},$$

where $\rho_{xy}^{raw}(H)$ is the raw Hall resistivity data. In the low-field region (below 60 kOe) the Hall resistivity $\rho_{xy}(H)$ shows a steep increase with the magnetic field H, and above that there is a change in slope, which signifies the presence of an additional component of the Hall resistivity. Considering the presence of the AHE and THE, the Hall resistivity can be written as

$$\rho_{xy}(H) = \rho_{xy}^{O} + \rho_{xy}^{AHE} + \rho_{xy}^{THE} = R_H H + R_s H \mu_0 M + \rho_{xy}^{THE},$$

where ρ_{xy}^{O}, ρ_{xy}^{AHE}, and ρ_{xy}^{THE} are the ordinary, anomalous, and topological components of the Hall resistivity, respectively. R_H and R_s are the ordinary and anomalous Hall coefficients, respectively. The value of R_H depends only on the carrier density of the sample and can be extracted from the linear fit of $\rho_{xy}(H)$ in the high-field regime (60$-$90 kOe). The pos-

itive slope indicates the charge carrier is the hole type. The calculated carrier density and mobility at 4 K turn out to be 2×10^{20} cm^{-3} and 1 cm^2/V s, respectively. After subtracting the ordinary Hall component ($\rho_{xy}^{O} = R_H H$), the additional component of the Hall resistivity at 4 K is plotted in Fig. 2(c). A similar procedure is followed to subtract the ordinary Hall component from the measured Hall data at other temperatures ($2-25$ K).

Figure 3 shows the magnetic field H dependence of the additional Hall component at different temperatures. In the temperature range of $10-25$ K, the additional component of Hall resistivity varies monotonically with the magnetic field H and gets saturated above 60 kOe, which corresponds to the presence of only the AHE. The strength of the AHE decreases as the temperature increases, and above 25 K it vanishes. In addition, it is seen that a small drop in the value of $\rho_{xy}^{AHE} + \rho_{xy}^{THE}$ occurs at 2 K and in the field range of $60-90$ kOe, which is attributed to the signature of the topological Hall effect, the details of which are discussed in the next section. In the electronic band picture, the AHE is attributed to the spin-orbit interaction induced anomalous velocity [10]. On the other hand, some theories postulated the AHE in terms of the spin-orbit interaction induced scattering modification, i.e., skew scattering [38] and the side jump mechanism [39], called the extrinsic mechanism. For a moderately conducting ($\sigma_{xx} < 10^4$ Ω^{-1} cm^{-1}) sample, the origin of the AHE cannot be related to the extrinsic mechanism via skew scattering or a side jump due to magnetic impurities [40,41]. Therefore, it must be of intrinsically related to Berry curvature in momentum space, which is clearer in the scaling analysis ρ_{xy}^{AHE} versus ρ_{xx} plot shown in Fig. 4(a). For ferromagnetic materials, the AHE ρ_{xy}^{AHE} is described by the empirical relation $\rho_{xy}^{AHE} = R_s H \mu_0 M$, where M is the net magnetization of the sample [41–43]. Recent observation of the AHE without notable magnetization in antiferromagnets has suggested that ferromagnetic ordering is not a necessary condition [44] and thus suggests a possible alternative origin of the AHE. In the context of $Eu_2Ir_2O_7(111)$ thin films, a recent synchrotron x-ray magnetic
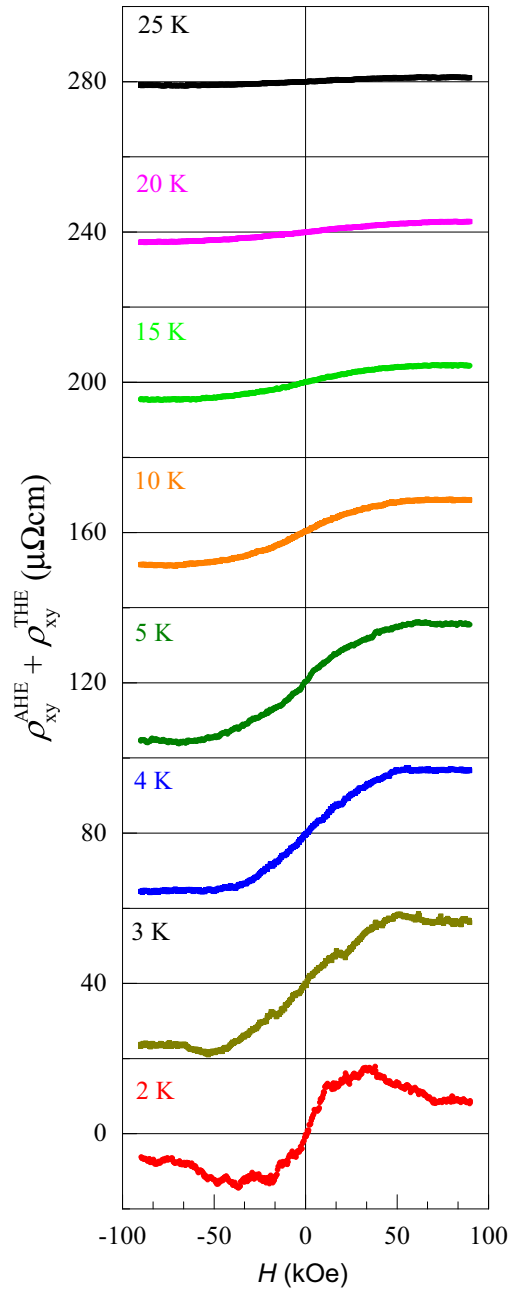
FIG. 3. Additional component of the Hall resistivity ($\rho_{xy}^{AHE} + \rho_{xy}^{THE}$) after subtracting the ordinary Hall resistivity component ρ_{xy}^{O} from the total Hall resistivity ρ_{xy} at different temperatures; the data are shifted vertically for visual clarity.

FIG. 4. (a) Scaling relationship between the saturated value of the anomalous Hall resistivity ρ_{Sat}^{AHE} and the longitudinal resistivity ρ_{xx} for Eu$_2$Ir$_2$O$_7$(111) thin films in the temperature range of 4−25 K. The blue line corresponds to $\rho_{Sat}^{AHE} \sim \rho_{xx}^{1.6}$ and indicates that the intrinsic Berry phase mechanism of AHE gets suppressed by disorder. (b) Color map of anomalous and topological Hall resistivities (after subtracting the ordinary Hall component) in the H-T plane. The black dashed curve corresponds to the boundary between the following two regions: (i) a low-temperature and high-field region, which corresponds to the magnetic WSM phase, and (ii) a high-temperature region where the AHE magnitude is extremely negligible, which corresponds to the semimetallic phase with AIAO spin ordering.

circular dichroism study revealed a very small net magnetization $\sim0.009(6)\mu_B$/Ir at a field strength of 60 kOe at 4 K to account for the observed AHE [45]. In the present study, the magnetic field dependent isothermal magnetization (M-H) curve at 5 K shows almost linear behavior [shown in Fig. S2(a)]; a similar behavior was observed in previous studies of single-crystal and polycrystalline Eu$_2$Ir$_2$O$_7$ [33,36,46,47], and a direct comparison between the field H dependence of $\rho_{xy}^{AHE}(H)$ and $M(H)$ at 5 K ruled out the magnetization origin of the AHE [shown in Fig. S2(b)], the details of which are discussed in the Supplementary Material [48].
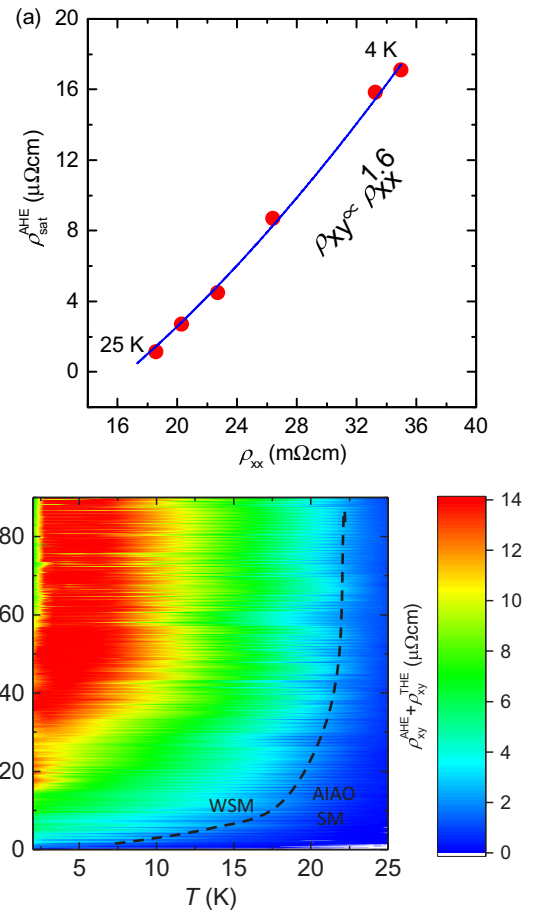
The observed hysteretic unconventional AHE on a relaxed Nd$_2$Ir$_2$O$_7$(111) thin film was explained in terms of the induced ferromagnetism at the domain walls of the AIAO/AOAI domains by Kim *et al.* [35]. Unlike for Nd$_2$Ir$_2$O$_7$, in the case of Eu$_2$Ir$_2$O$_7$ the domain-wall conductance is negligible [45]. Note that recent reports on Nd$_2$Ir$_2$O$_7$(111) [49] and Pr$_2$Ir$_2$O$_7$(111) [50] thin films revealed Berry curvature induced AHE. A nonlinear Hall effect also arises in Nd$_2$Ir$_2$O$_7$ single crystals due to the multiple magnetic field H induced topological phases with varying numbers of Weyl nodes [36,51]. The Weyl nodes act as sources or drains of the Berry curvature in momentum space [6,9]. Therefore, in the case of Eu$_2$Ir$_2$O$_7$(111) thin films having AIAO/AIAO antiferromagnetic ordering and no domain-wall conductance, the observed large AHE ($\sim$15 $\mu\Omega$ cm at 4 K) can be explained

in terms of the Berry curvature $\Omega(\vec{k})$ of the filled bands in momentum space [45,52]. The anomalous Hall conductivity $\sigma_{xy}^{\mathrm{AHE}}$ is proportional to the integral of the Berry curvature over the whole Brillouin zone (BZ), $\sigma_{xy}^{\mathrm{AHE}} \sim \int_{\mathrm{BZ}} \Omega(\vec{k}) d^3\vec{k}$. A large contribution of the Berry curvature comes from the band-crossing points or Weyl points. As the upper and lower bands of the crossing points have equal and opposite Berry curvatures, the Berry curvature contribution to $\sigma_{xy}^{\mathrm{AHE}}$ will be strongly enhanced when the crossing (Weyl) points lie on the Fermi surface, so only one of the bands will be occupied. The diverging nature of the resistivity as shown in Fig. 2(a) ($\rho_{xx} \rightarrow \infty$ when $T \rightarrow 0$) suggests a vanishing density of states in the Fermi level, which indicates the Fermi level lies near the crossing points [6]. Further, a recent band structure calculation of $Eu_2Ir_2O_7(111)$ thin films with resistivity values similar to those reported in the present study showed that the Fermi level lies very close to the band-crossing Weyl points [45]. For time-reversal symmetry-preserved system, $\Omega(-\vec{k}) = -\Omega(\vec{k})$. Therefore, the integration of the Berry curvature over the whole BZ will cancel out; as a result, the net anomalous Hall effect will be suppressed. In the present case, the AIAO/AOAI AFM ordering of $Eu_2Ir_2O_7(111)$ thin films breaks the time-reversal symmetry and causes a finite AHE. In general, for cubic crystal with twofold rotation, C_2 symmetries about the x, y, or z axis suppress the Berry curvature effect, as $\Omega(\vec{k})$ is canceled by $\Omega(C_2\vec{k})$. Therefore, for bulk $Eu_2Ir_2O_7$, in the presence of all three C_2 symmetries the net $\Omega(\vec{k})$ contribution remains hidden. In contrast, for $Eu_2Ir_2O_7(111)$ thin films with biaxial compressive strain [as shown in Fig. 1(c)], all three C_2 symmetries break; as a result a finite net $\Omega(\vec{k})$ contribution emerges and causes a large AHE. This is consistent with the theoretical calculations, which expect a large AHE for pyrochlore iridate thin films grown along the [111] direction with an AIAO/AOAI spin structure [28,45]. To understand the underlying mechanism of the AHE in terms of the scaling analysis ($\rho_{xy}^{\mathrm{AHE}} \propto \rho_{xx}^{\alpha}$), the saturated value of the anomalous Hall resistivity $\rho_{\mathrm{Sat}}^{\mathrm{AHE}}$ versus the longitudinal resistivity ρ_{xx} is plotted in Fig. 4(a) in the temperature range of $4-25$ K. The blue line corresponds to a fit of the experimental data (red circles); it is seen that $\rho_{\mathrm{Sat}}^{\mathrm{AHE}}$ varies as $\rho_{\mathrm{Sat}}^{\mathrm{AHE}} \propto \rho_{xx}^{1.6}$, which signifies that the intrinsic Berry phase origin of the AHE is suppressed by disorder [40,41,49,53,54]. Figure 4(b) shows the contour plot of $\rho_{xy}^{\mathrm{AHE}} + \rho_{xy}^{\mathrm{THE}}$ in the H-T plane. In the low-temperature and high-field region, the AHE has a high magnitude, which corresponds to the presence of a magnetic WSM (AIAO WSM). On the other hand, in the high-temperature region (above 25 K) the AHE vanishes even at high magnetic field, but the AIAO/AOAI AFM order is present, so it is called an AIAO semimetal (AIAO SM). The black dashed curve in Fig. 4(b) separates the two regions in the H-T plane.

D. Topological Hall effects

In addition to the AHE, a humplike feature can be observed around 40 kOe in the 2 K Hall resistivity data [in Fig. 3(a)], which indicates the presence of the THE. The size of the humplike feature decreases as the temperature increases and vanishes above 5 K. This kind of additional component of the AHE ($\Delta\rho^{\mathrm{AHE}}$) which varies nonmonotonically with magnetic field was also observed in La-doped $EuTiO_3$ (001) films; it was attributed to the Berry curvature contribution of multiple Weyl nodes in the conduction band [53]. But in Sm-doped $EuTiO_3(001)$ thin films the observed additional humplike feature was assigned to the THE and was explained in terms of noncolinear spin structure [55,56]. The THE also occurs in topologically protected skyrmions like spin texture in MnSi or [57,58] pyrochlore lattices with noncoplanar chiral spin structure [29–32]. The noncoplanar AIAO/AOAI spin structure in $Eu_2Ir_2O_7(111)$ thin films can cause a nonzero scalar spin chirality $\chi_{ijk} = \mathbf{S}_i \cdot (\mathbf{S}_j \times \mathbf{S}_k)$, where $\mathbf{S}_i$, $\mathbf{S}_j$, and $\mathbf{S}_k$ are the static spins at sites i, j, and k, respectively. Due to this nonzero χ_{ijk} (real-space Berry curvature) conduction electrons experience an additional fictitious magnetic field, which causes the THE. When a conduction electron traverses three neighboring static spins $\mathbf{S}_1$, $\mathbf{S}_2$, and $\mathbf{S}_3$ and completes a loop $1 \rightarrow 2 \rightarrow 3 \rightarrow 1$, the Berry curvature acquired by it is equal to half of the solid angle subtended by those three static spins. Figure 5(a) shows a schematic of the solid angle subtended by the three noncoplanar spins of the AOAI (domain B) magnetic order, and the blue arrow indicates the fictitious magnetic field experienced by the conduction electron due to the real-space Berry curvature.

To check the field H and temperature T evolution of the topological Hall resistivity ρ_{xy}^{THE}, the AHE component needs to be subtracted properly at each temperature T. We used mathematical operation to help capture the AHE component correctly [59]. For the 10 K data [shown in Fig. 5(b)], where only the anomalous component is present, we adopted a higher-order empirical odd polynomial function of H to capture the smooth variation of AHE with magnetic field H [fitted curve shown by the solid red line in Fig. 5(b)] [49,59]. Similarly, the AHE component at 2 K is captured by using the odd polynomial of H and then subtracted to extract the THE component. Figure 5(c) shows the AHE+THE data at 2 K; the solid black line corresponds to the simulated AHE at 2 K. The field H dependence of ρ_{xy}^{THE} at 2 K after subtracting the AHE component is shown in Fig. 5(d). It can be seen that in the low-field region below 40 kOe the THE increases with an increase in field, whereas in the high-field region, it decreases as field increases. The spin structures of domain A (AIAO) and domain B (AOAI) suggest that at zero magnetic field ($H = 0$), they will have equal and opposite scalar spin chirality χ_{ijk}; therefore, the net Berry phase acquired by the conduction electrons will be canceled out and causes no THE. On the other hand, in the low-field regime ($H < 40$ kOe), a finite applied field H will cause canting of the AIAO/AIAO spin structure. Since the field-induced spin canting is not the same for AIAO (domain A) and AOAI (domain B), a net finite spin chirality induced THE occurs and increases with the magnetic field before getting saturated around 40 kOe. In the higher magnetic field regime ($H > 40$ kOe), the spins $\mathbf{S}_i$ will tend to align along the field direction, so the spin chirality induced THE decreases with the magnetic field [29,32,60].
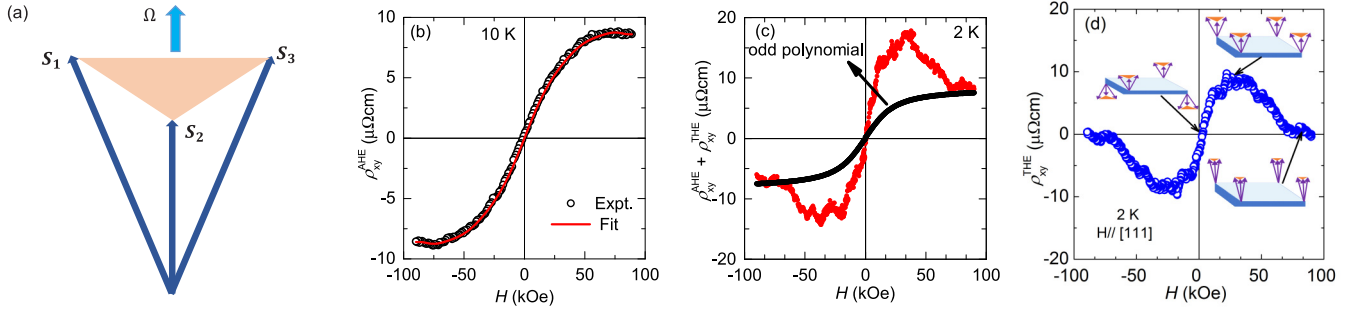
FIG. 5. (a) Schematic of the solid angle Ω, subtended by three noncoplanar neighboring spins, $\mathbf{S}_1$, $\mathbf{S}_2$, and $\mathbf{S}_3$, of domains A and B, resulting in an effective magnetic field, shown by the blue arrow. (b) Black open circles represent the anomalous Hall resistivity data at 10 K; a higher-order polynomial has been fitted to capture the smooth variation of the AHE with the magnetic field (the solid red line represents the fitting). (c) Anomalous and topological components of the Hall resistivity at 2 K. The black curve represents the higher-order polynomial; we scaled it to capture the anomalous component of the Hall resistivity. (d) Topological component of the Hall resistivity data at 2 K after subtracting the anomalous component from (c). Inset schematics show the behavior of spin triads at different magnetic field strengths, as indicated by black arrows.

E. Magnetoresistance

The coupling of the conduction electrons to the underlying magnetic structure can be captured by magnetotransport studies. Figure 6(a) shows the magnetic field H dependence of the MR in the temperature range of 2−10 K. The MR(%) is calculated as

$$\text{MR}(\%) = \frac{\rho_{xx}(H) - \rho_{xx}(0)}{\rho_{xx}(0)} \times 100,$$

where $\rho_{xx}(H)$ and $\rho_{xx}(0)$ are the longitudinal resistivities with magnetic field H and without any magnetic field, respectively. In the temperature region of 2−5 K the sample shows large nonsaturating negative MR up to the highest measured field of 90 kOe, and no hysteresis was observed between field H sweep-up and sweep-down processes. The magnitude of negative MR increases with a decrease in temperature (9.8% at 90 kOe for 2 K). An earlier thin-film study by Fujita *et al.* also reported negative MR, but the magnitude of MR% (0.5% at 90 kOe for 2 K) was less than that in the present study [61]. This MR behavior is consistent with the bulk polycrystal sample, which shows negative MR [33], but some other studies showed positive MR at the lowest measured temperature [46,62,63]. This negative MR appears due to the field H induced modification of the spin chirality (spin canting) $\chi_{ijk} = \mathbf{S}_i \cdot (\mathbf{S}_j \times \mathbf{S}_k)$ of the static spins in the AIAO/AOAI spin structure [33,61]. It is observed that in the low-field region below 40 kOe, the MR varies quadratically with field ($\propto H^2$), but in the high-field region, MR varies almost linearly and remains unsaturated up to the highest measured field of 90 kOe. For clear visualization and to find the field region at which crossover from quadratic to linear MR occurs we plot the field derivative $d\,\text{MR}/dH$ for 2−10 K in Fig. 6(b). It can clearly be seen that for the 2−5 K data the slope varies almost linearly up to 30 kOe (corresponding to quadratic MR), and above 50 kOe the slope gets saturated (corresponding to linear MR). The crossover occurs around a field strength of 40 kOe, at which the THE signal also becomes maximum [shown in
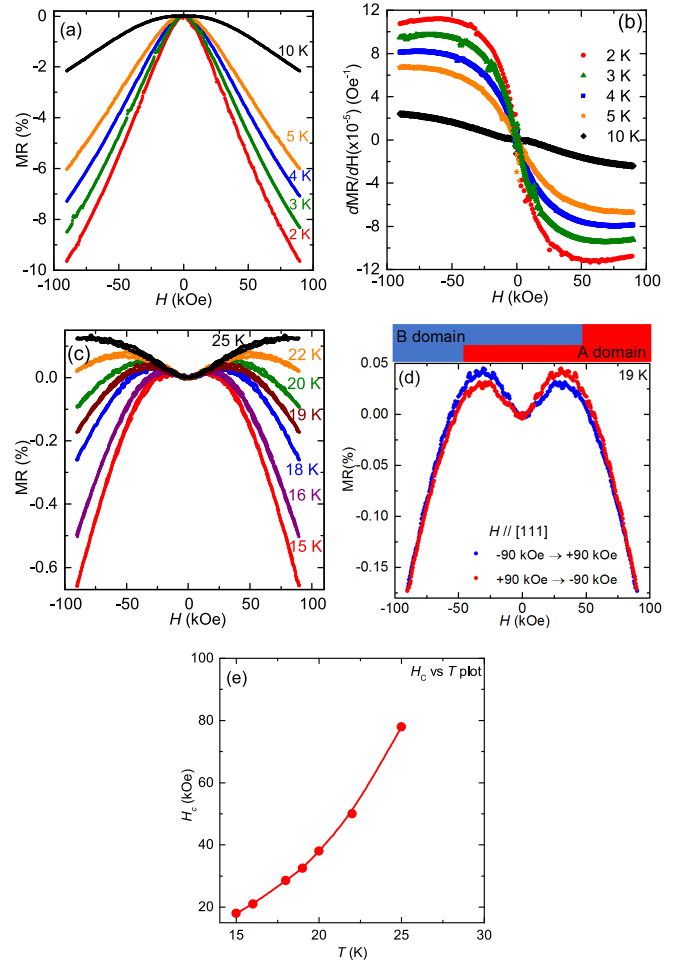

FIG. 6. Magnetic field H dependence of (a) nonhysteretic MR at low temperatures and (b) its field derivative plot in the temperature range of 2−10 K. (c) Hysteretic MR at different fixed temperatures in the range of 15−25 K. (d) Magnified plot of the MR data at 19 K with the applied field H along the [111] direction. (e) Switching field H_C vs temperature plot in the range of 15−25 K.

Fig. 5(d)]. We thus hypothesize that the change in net spin chirality (spin canting) $\chi_{ijk} = \mathbf{S}_i.(\mathbf{S}_j \times \mathbf{S}_k)$ of the static spins in the noncoplanar AIAO/AOAI spin structure has a role to play in the observed quadratic to linear crossover in MR.

Figure 6(c) shows magnetic field H dependence of the MR data in the intermediate-temperature region of $15-25$ K. It can be seen that there is small positive MR in the low-field region, and as the field strength increases, a crossover from positive to negative MR occurs. In addition, the MR curves show a finite hysteresis between field-increasing and -decreasing processes. For clarity, MR data at 19 K are separately plotted in Fig. 6(d)), which shows a finite hysteresis loop around $H \sim 35$ kOe, and the loop completely closes in the high-field region. Upon close examination around the field regime of $\sim +35$ kOe, it can be seen that the MR(%) is higher for the field sweep-down process (denoted by the red circles) than the field sweep-up process (blue circles), and the trend is opposite in the negative field regime. Such a butterfly-type hysteresis loop has also been observed in pressure-tuned $Nd_2Ir_2O_7$ single crystals [36].

The asymmetry in MR(%) and hysteresis can be explained by the presence of two types of magnetic domains (domains A and B) of $Eu_2Ir_2O_7$ in its AIAO/AOAI ordered state. In zero magnetic field ($H = 0$), the sample will have equal proportions of domains A and B, but the application of field can cause an imbalance in the domain proportions. Previous studies showed that if a sample is cooled under an applied magnetic field H along the [111] direction, domain A will get stabilized and that for a negative field direction the stabilization will occur in the domain B [37,61]. This means the AIAO (domain A) and AOAI (domain B) are energetically favorable for the applied positive and negative magnetic fields, respectively. The alignment of only one kind of domain configuration causes asymmetric MR. For the presence of only domain A the resistance value is higher on the positive side of the field than on the negative side of the field, and the trend is opposite if only domain B exists [37,61]. Therefore, the butterfly-type hysteresis in MR [shown in Fig. 6(d)] can be explained by the imbalance of domains A and B in the positive and negative field regions. Although at zero magnetic field ($H = 0$) both domains A and B will be present in equal proportion, for an applied positive field along the [111] direction, due to spin flipping some of domain B (AOAI) will be converted to domain A (AIAO). Therefore, in the field-decreasing process ($+90 \rightarrow -90$ kOe) the sample will have excess domain A over domain B, which causes asymmetry in MR. Similarly, for an applied negative field along the [111] direction, some of domain A (AIAO) will get converted to domain B (AOAI), and therefore, in the field-increasing process ($-90 \rightarrow +90$ kOe) the excess domain B over domain A will cause an opposite asymmetry. In essence, the field-induced domain imbalance (switching from AIAO to AOAI or AOAI to AIAO) causes finite hysteresis in MR. With an increase in temperature to 25 K and above, MR (hysteretic) remains positive up to the highest measured field of 90 kOe. However, the hysteresis in MR completely vanishes above 90 K (higher-temperature MR data are shown in the Supplemental Material [48]), which corresponds to the magnetic ordering temperature [the same as T_{MI} observed in Fig. 2(a)]. For a qualitative understanding and estimation of the field-induced

(spin flipping) partial domain switching mechanism, from 15 K onward we plot the switching field H_C (at which the magnetic field crossover from positive to negative MR occurs) vs temperature in Fig. 6(e). This H_C value gives an indirect measure (probability) of the number of domain B (A) switches to domain A (B) for an applied positive (negative) magnetic field. It can be seen that the H_C value continuously increases as temperature increases in the range of $15-25$ K, and above 30 K we could not determine the H_C value as the MR remains positive up to the highest measured field strength of 90 kOe. This H_C behavior suggests that as the temperature increases, the domain switching probability also increases, starting from 15 K. Therefore, our magnetotransport studies suggests the MR phenomenon reflects the magnetic spin structure as well as the magnetic domain structure.

The presence of field-induced irreversibility (hysteresis) from 15 K onward and nonhysteretic MR at lower temperature (below 15 K) is an intriguing phenomenon. It indicates a subtle interplay between exchange energy and Zeeman energy as a function of magnetic field H and temperature T. In the low-temperature region ($2-10$ K), the antiferromagnetic exchange energy between AIAO Ir^{4+} moments dominates over the Zeeman energy and gives rise to no-field-induced domain switching; only canting of the spin occurs. However, above 10 K the Zeeman energy competes with the exchange energy, which causes field H induced flipping of the spin structure (domain switching). This hysteretic MR behavior emphasizes the role of the Zeeman energy in Ir domain switching of pyrochlore iridate ($Eu_2Ir_2O_7$) thin films with a single magnetic sublattice. The magnetoresistance study indicates that in the low-temperature region ($2-5$ K) both domains A (AIAO) and B (AOAI) are robust against the external applied magnetic field. This robust AIAO/AOAI noncoplanar spin structure generates finite scalar spin chirality, which causes large THE and negative MR in this temperature region ($2-5$ K). As the temperature increases to 15 K and above, the field-induced (spin flipping) partial domain switching starts, so the THE vanishes. However, momentum space Berry curvature induced AHE persists up to 25 K. The presence of finite hysteresis in MR signifies persistence of AIAO/AOAI AFM ordering of $Eu_2Ir_2O_7$ up to the metal-semimetal transition temperature at 90 K, which indicates the spin ordering of Ir^{4+} correlates with the scattering of the conduction electrons. The presence of hysteresis in MR (ρ_{xx}) and the absence of the same in AHE (ρ_{xy}^{AHE}) in the temperature range of $10-25$ K signifies that the origins of these effects have different underlying mechanisms. The AHE ρ_{xy}^{AHE} and its field variation are governed by the Berry curvature in momentum space associated with the presence of Weyl nodes in an electronic band structure. However, the hysteretic MR above 10 K occurs due to the field-induced domain modifications of the Ir^{4+} $5d$ moments. Therefore, the absence of hysteresis in the AHE observed in the temperature range of $10-25$ K, although it is present in MR, rules out the magnetic domain switching origin of the AHE.

IV. CONCLUSION

We observed a large anomalous Hall effect ($\rho_{xy}^{AHE} \sim 15$ $\mu\Omega$ cm at 4 K) in $Eu_2Ir_2O_7(111)$ epitaxial thin films.

The observed AHE is explained in terms of the Berry curvature in momentum space associated with Weyl nodes, which indirectly confirms the theoretically predicted magnetic Weyl semimetallic phase in $Eu_2Ir_2O_7$. In addition, the AIAO/AOAI noncoplanar spin structure causes a scalar spin chirality induced large topological Hall effect ($\rho_{xy}^{THE} \sim 10 \ \mu\Omega$ cm at 2 K) and negative magnetoresistance in the low-temperature regime (below 5 K). These observations suggest that the $Eu_2Ir_2O_7$(111) thin film is a fertile ground to host both real- and momentum space topological phenomena. Further, the hysteretic MR revealed field-induced modification of the AIAO/AOAI domain configuration. For in-depth understanding of the domain structure, future magnetic field H and temperature T dependent neutron and x-ray studies are needed.

ACKNOWLEDGMENTS

[1] W. Witczak-Krempa, G. Chen, Y. B. Kim, and L. Balents, Annu. Rev. Condens. Matter Phys. **5**, 57 (2014).

[2] D. Pesin and L. Balents, Nat. Phys. **6**, 376 (2010).

[3] B. Yan and C. Felser, Annu. Rev. Condens. Matter Phys. **8**, 337 (2017).

[4] Y. Tokura, K. Yasuda, and A. Tsukazaki, Nat. Rev. Phys. **1**, 126 (2019).

[5] Y. Tokura, M. Kawasaki, and N. Nagaosa, Nat. Phys. **13**, 1056 (2017).

[6] X. Wan, A. M. Turner, A. Vishwanath, and S. Y. Savrasov, Phys. Rev. B **83**, 205101 (2011).

[7] H. Weng, C. Fang, Z. Fang, B. A. Bernevig, and X. Dai, Phys. Rev. X **5**, 011029 (2015).

[8] N. P. Armitage, E. J. Mele, and A. Vishwanath, Rev. Mod. Phys. **90**, 015001 (2018).

[9] Z. Fang, N. Nagaosa, K. S. Takahashi, A. Asamitsu, R. Mathieu, T. Ogasawara, H. Yamada, M. Kawasaki, Y. Tokura, and K. Terakura, Science **302**, 92 (2003).

[10] R. Karplus and J. M. Luttinger, Phys. Rev. **95**, 1154 (1954).

[11] F. D. M. Haldane, Phys. Rev. Lett. **93**, 206602 (2004).

[12] M. Ikhlas, T. Tomita, T. Koretsune, M. T. Suzuki, D. Nishio-Hamane, R. Arita, Y. Otani, and S. Nakatsuji, Nat. Phys. **13**, 1085 (2017).

[13] H. B. Nielsen and M. Ninomiya, Phys. Lett. B **130**, 389 (1983).

[14] K. Y. Yang, Y. M. Lu, and Y. Ran, Phys. Rev. B **84**, 075129 (2011).

[15] A. A. Burkov and L. Balents, Phys. Rev. Lett. **107**, 127205 (2011).

[16] E. Liu, Y. Sun, N. Kumar, L. Muechler, A. Sun, L. Jiao, S. Y. Yang, D. Liu, A. Liang, Q. Xu, J. Kroder, V. Süß, H. Borrmann, C. Shekhar, Z. Wang, C. Xi, W. Wang, W. Schnelle, S. Wirth, Y. Chen, S. T. B. Goennenwein, and C. Felser, Nat. Phys. **14**, 1125 (2018).

[17] D. F. Liu, A. J. Liang, E. K. Liu, Q. N. Xu, Y. W. Li, C. Chen, D. Pei, W. J. Shi, S. K. Mo, P. Dudin, T. Kim, C. Cacho, G. Li, Y. Sun, L. X. Yang, Z. K. Liu, S. S. P. Parkin, C. Felser, and Y. L. Chen, Science **365**, 1282 (2019).

[18] I. Belopolski, K. Manna, D. S. Sanchez, G. Chang, B. Ernst, J. Yin, S. S. Zhang, T. Cochran, N. Shumiya, H. Zheng, B. Sing, G. Bian, D. Multer, M. Litskevich, X. Zhou, S.-M. Huang, B. Wang, T.-R. Chang, S.-Y. Xu, A. Bansil, C. Felser, H. Lin, and M. H. Hasan, Science **365**, 1278 (2019).

[19] K. Kuroda, T. Tomita, M.-T. Suzuki, C. Bareille, A. A. Nugroho, P. Goswami, M. Ochi, M. Ikhlas, M. Nakayama, S.

Akebi, R. Noguchi, R. Ishii, N. Inami, K. Ono, H. Kumigashira, A. Varykhalov, T. Muro, T. Koretsume, R. Arita, S. Shin, T. Kondo, and S. Nakatsuji, Nat. Mater. **16**, 1090 (2017).

[20] P. Hosur, S. A. Parameswaran, and A. Vishwanath, Phys. Rev. Lett. **108**, 046602 (2012).

[21] S. T. Bramwell and M. J. Harris, J. Phys.: Condens. Matter **10**, L215 (1998).

[22] A. B. Sushkov, J. B. Hofmann, G. S. Jenkins, J. Ishikawa, S. Nakatsuji, S. Das Sarma, and H. D. Drew, Phys. Rev. B **92**, 241108(R) (2015).

[23] A. A. Burkov, Annu. Rev. Condens. Matter Phys. **9**, 359 (2018).

[24] A. A. Burkov, Phys. Rev. Lett. **113**, 187202 (2014).

[25] J. F. Steiner, A. V. Andreev, and D. A. Pesin, Phys. Rev. Lett. **119**, 036601 (2017).

[26] S. Zhao, J. M. Mackie, D. E. MacLaughlin, O. O. Bernal, J. J. Ishikawa, Y. Ohta, and S. Nakatsuji, Phys. Rev. B **83**, 180402(R) (2011).

[27] H. Sagayama, D. Uematsu, T. Arima, K. Sugimoto, J. J. Ishikawa, E. O'Farrell, and S. Nakatsuji, Phys. Rev. B **87**, 100403(R) (2013).

[28] B. J. Yang and N. Nagaosa, Phys. Rev. Lett. **112**, 246402 (2014).

[29] Y. Machida, S. Nakatsuji, Y. Maeno, T. Tayama, T. Sakakibara, and S. Onoda, Phys. Rev. Lett. **98**, 057203 (2007).

[30] Y. Taguchi, T. Sasaki, S. Awaji, Y. Iwasa, T. Tayama, T. Sakakibara, S. Iguchi, T. Ito, and Y. Tokura, Phys. Rev. Lett. **90**, 257202 (2003).

[31] M. Udagawa and R. Moessner, Phys. Rev. Lett. **111**, 036602 (2013).

[32] Y. Taguchi, Y. Oohara, H. Yoshizawa, N. Nagaosa, and Y. Tokura, Science **291**, 2573 (2001).

[33] S. Mondal, M. Modak, B. Maji, M. K. Ray, S. Mandal, S. K. Mandal, M. Sardar, and S. Banerjee, Phys. Rev. B **102**, 155139 (2020).

[34] P. Bruno, V. K. Dugaev, and M. Taillefumier, Phys. Rev. Lett. **93**, 096806 (2004).

[35] W. J. Kim, J. H. Gruenewald, T. Oh, S. Cheon, B. Kim, O. B. Korneta, H. Cho, D. Lee, Y. Kim, M. Kim, J.-G. Park, B.-J. Yang, A. Seo, and T. W. Noh, Phys. Rev. B **98**, 125103 (2018).

[36] K. Ueda, R. Kaneko, H. Ishizuka, J. Fujioka, N. Nagaosa, and Y. Tokura, Nat. Commun. **9**, 3032 (2018).

[37] M. Ghosh, S. G. Bhat, A. Pal, and P. S. A. Kumar, J. Phys.: Condens. Matter **34**, 165701 (2022).

[38] J. Smit, Physica (Amsterdam) **24**, 39 (1958).

[39] L. Berger, Phys. Rev. B **2**, 4559 (1970).

[40] S. Onoda, N. Sugimoto, and N. Nagaosa, Phys. Rev. Lett. **97**, 126602 (2006).

[41] N. Nagaosa, J. Sinova, S. Onoda, A. H. MacDonald, and N. P. Ong, Rev. Mod. Phys. **82**, 1539 (2010).

[42] E. H. Hall, London, Edinburgh, Dublin Philos. Mag. J. Sci. **12**, 157 (1881).

[43] E. M. Pugh, Phys. Rev. **36**, 1503 (1930).

[44] N. Kiyohara, T. Tomita, and S. Nakatsuji, Phys. Rev. Appl. **5**, 064009 (2016).

[45] X. Liu, S. Fang, Y. Fu, W. Ge, M. Kareev, J. W. Kim, Y. Choi, E. Karapetrova, Q. Zhang, L. Gu, E.-S. Choi, F. Wen, J. H. Wilson, G. Fabbris, P. J. Ryan, J. W. Freeland, D. Haskel, W. Wu, J. H. Pixley, and J. Chakhalian, Phys. Rev. Lett. **127**, 277204 (2021).

[46] L. Xu, G. Gong, C. Zhao, X. Song, S. Yuan, Songliu, and Z. Tian, J. Phys. Chem. C **124**, 22656 (2020).

[47] A. Banerjee, J. Sannigrahi, S. Giri, and S. Majumdar, Phys. Rev. B **96**, 224426 (2017).

[48] See Supplemental Material at http://link.aps.org/supplemental/10.1103/PhysRevB.106.085139 for details about high-temperature (30–150 K) magnetoresistance, isothermal magnetization and its comparison with anomalous Hall resistivity at 5 K, Hall resistivity data at 30–150 K, and the temperature dependence of the carrier density and mobility.

[49] W. J. Kim, T. Oh, J. Song, E. K. Ko, Y. Li, J. Mun, B. Kim, J. Son, Z. Yang, Y. Kohama, M. Kim, B. J. Yang, and T. W. Noh, Sci. Adv. **6**, eabb1539 (2020).

[50] Y. Li, T. Oh, J. Son, J. Song, M. K. Kim, D. Song, S. Kim, S. H. Chang, C. Kim, B.-J. Yang, and T. W. Noh, Adv. Mater. **33**, 2008528 (2021).

[51] K. Ueda, T. Oh, B.-J. Yang, R. Kaneko, J. Fujioka, N. Nagaosa, and Y. Tokura, Nat. Commun. **8**, 15515 (2017).

[52] T. Liang, J. Lin, Q. Gibson, S. Kushwaha, M. Liu, W. Wang, H. Xiong, J. A. Sobota, M. Hashimoto, P. S. Kirchmann, Z.-X. Shen, R. J. Cava, and N. P. Ong, Nat. Phys. **14**, 451 (2018).

[53] K. S. Takahashi, H. Ishizuka, T. Murata, O. Y. Wang, Y. Tokura, N. Nagaosa, and M. Kawasaki, Sci. Adv. **4**, eaar7880 (2018).

[54] T. Fukumura, H. Toyosaki, K. Ueno, M. Nakano, T. Yamasaki, and M. Kawasaki, Jpn. J. Appl. Phys. **46**, L642 (2007).

[55] K. Ahadi, L. Galletti, and S. Stemmer, Appl. Phys. Lett. **111**, 172403 (2017).

[56] K. Ahadi, Z. Gui, Z. Porter, J. W. Lynn, Z. Xu, S. D. Wilson, A. Janotti, and S. Stemmer, APL Mater. **6**, 056105 (2018).

[57] A. Neubauer, C. Pfleiderer, B. Binz, A. Rosch, R. Ritz, P. G. Niklowitz, and P. Boni, Phys. Rev. Lett. **102**, 186602 (2009).

[58] Y. Fujishiro, N. Kanazawa, T. Nakajima, X. Z. Yu, K. Ohishi, Y. Kawamura, K. Kakurai, T. Arima, H. Mitamura, A. Miyake, K. Akiba, M. Tokunaga, A. Matsuo, K. Kindo, T. Koretsune, R. Arita, and Y. Tokura, Nat. Commun. **10**, 1059 (2019).

[59] D. Liang, J. P. DeGrave, M. J. Stolt, Y. Tokura, and S. Jin, Nat. Commun. **6**, 8217 (2015).

[60] W. Wang, M. W. Daniels, Z. Liao, Y. Zhao, J. Wang, G. Koster, G. Rijnders, C. Z. Chang, D. Xiao, and W. Wu, Nat. Mater. **18**, 1054 (2019).

[61] T. C. Fujita, Y. Kozuka, M. Uchida, A. Tsukazaki, T. Arima, and M. Kawasaki, Sci. Rep. **5**, 9711 (2015).

[62] K. Matsuhira, M. Tokunaga, M. Wakeshima, Y. Hinatsu, and S. Takagi, J. Phys. Soc. Jpn. **82**, 023706 (2013).

[63] F. F. Tafti, J. J. Ishikawa, A. McCollam, S. Nakatsuji, and S. R. Julian, Phys. Rev. B **85**, 205104 (2012).